Directed Particle Transport via Reconfigurable Fiber Networks

Katharina Cu, Anke Steier, Marvin Klaiber, Matthias Franzreb, and Joerg Lahann*

Mass transport limitations of particulates within conventional microanalytical systems are often cited as the root cause for low sensitivity but can be overcome by directed analyte transport, such as via biomolecular motors or gradient surfaces. An ongoing challenge is the development of materials that are passive in nature (i.e., no external power source required), but can reconfigure to perform work, such as transporting particle-based analytes. Mimicking biology's concepts of autonomous and reconfigurable materials systems, like the *Drosera capensis* leaf, reconfigurable fiber networks that effectively concentrate particulates within a localized spot that can act as a detection patch are developed. These networks, prepared by electrohydrodynamic co-jetting, draw their reconfigurability from a bicompartmental fiber architecture. Upon exposure to neutral pH, a differential swelling of both fiber compartments gives rise to interfacial tension and ultimately results in shape reconfiguration of the fiber network. Compared to free particles, the reconfigurable fiber networks display a 57-fold increase in analyte detectability, average transport efficiencies of 91.9 ± 2.4%, and separation selectivity between different surface properties of 95 ± 3%. The integration of biomimetic materials into microanalytical systems, exemplified in this study, offers ample opportunities to design novel and effective detection schemes that circumvent mass transport limitations.

1. Introduction

Over the last few decades, significant progress has been made in the field of microanalytical systems.[1] Their compact size and highly integrated architecture enable analyte detection from low and diluted sample volumes. One advantage of a reduced sensing area is the increased sensing resolution.[2] However, at the same time, a small sensing area significantly reduces the probability of an analyte reaching the detection patch as the analyte will have to diffuse through a 3D sample space.[2b,3] An analyte depletion adjacent to the detection patch leads to a less accurate detection output.[4] Mass transport, therefore, limits the analyte collection and presents the bottleneck of current microanalytical systems.[4c,5] Various research groups have proposed directed transport based on motor proteins or chemically and topographically patterned protein tracks to speed up the collection time.[6] The downside of these complex materials, however, is their time-consuming and expensive production, which limits the scalability of these biomolecular motor-based devices.[7] Surface gradients, where the surfaces change their physical or chemical properties over a given distance, have also been proposed to overcome mass transport limitations by direct transport.[2a,8] However, the disadvantages of such platforms can be possible surface irregularities[9] and non-specificity.[10] Moreover, limited repeatability due to many parameters involved in optimizing conditions can further restrict the scalability.[11]

Nature has inspired the design of reconfigurable materials systems.[12] For example, the leaves of the carnivorous plant, *Drosera capensis*, undergo a bending motion due to their asymmetric cellular architecture. Upon tactile sensation, the upper and more rigid cell layer expands to a lesser extent than the other (**Figure 1**, top).[13] Analogous to the leaf's asymmetry, first approaches have been explored in the past, in which architectural inhomogeneity in combination with mechanical mismatches are responsible for shape reconfigurability.[14] The mechanical properties of materials can vary due to different molecular weights, crosslinking, and crystallinity.[15] Shape-shifting systems with distinct properties are fabricated in the form of bilayer or patterned films,[14e,16] fibers,[17] or particles.[18] Multicompartmental microcylinders, for instance, fabricated via electrohydrodynamic (EHD) co-jetting, can undergo defined shape reconfiguration, such as bending, toggling, or shape-shifting into spheres.[19] However, to our knowledge, none of these systems have been systematically applied in the analytical field since most of the systems reconfigure in an undirected manner.

Mimicking nature's approach, we designed reconfigurable fiber network structures that actively transport to and accumulate in a

K. Cu, A. Steier, M. Klaiber, M. Franzreb, J. Lahann
Institute of Functional Interfaces
Karlsruhe Institute of Technology
76344 Eggenstein-Leopoldshafen, Germany
E-mail: lahann@umich.edu

J. Lahann
Biointerfaces Institute
Departments of Chemical Engineering
Materials Science and Engineering, and Biomedical Engineering,
and the Macromolecular Science and Engineering Program
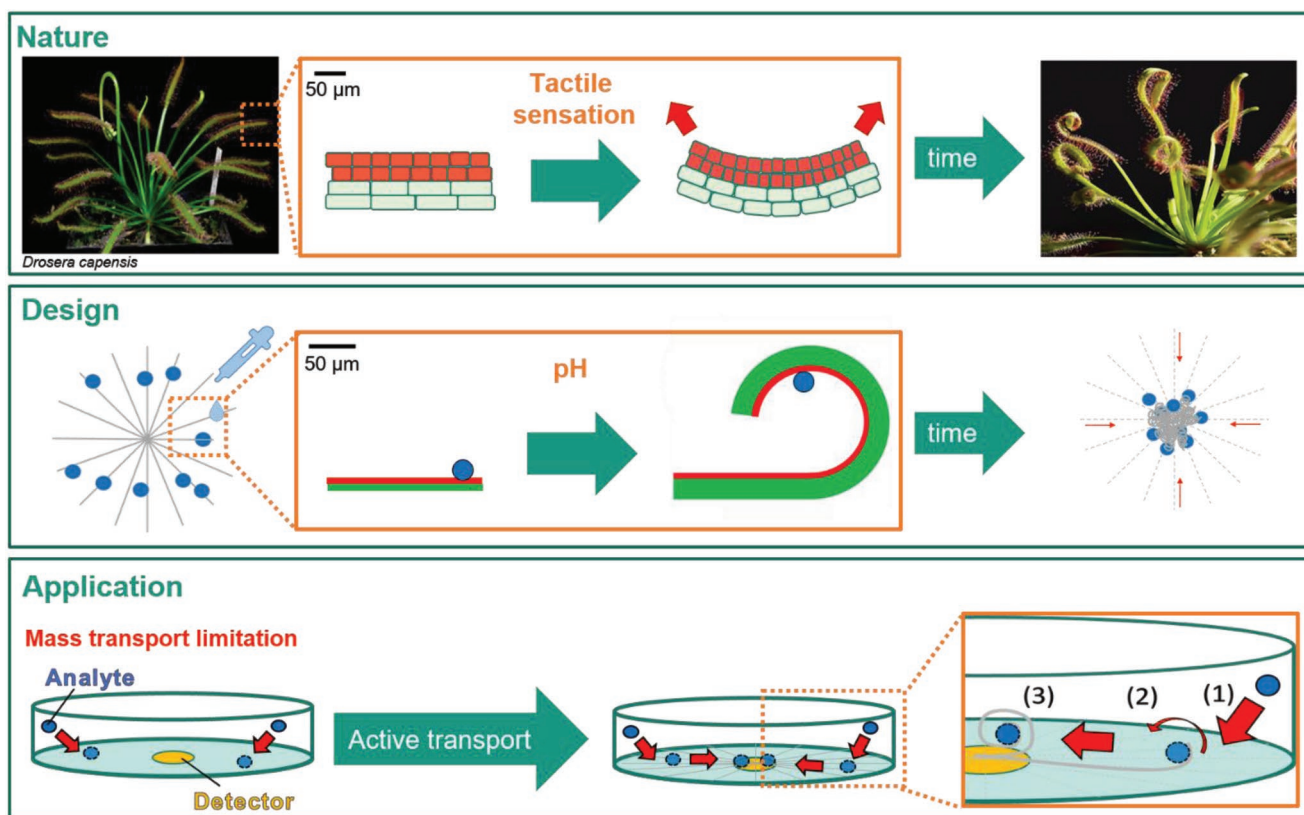University of Michigan
Ann Arbor, MI 48109, USA

Figure 1. Design of the biomimetic actuator as microanalytical system. Top: Inspiration from the carnivorous plant, *Drosera capsensis*. Its anisotropic cellular leaf architecture is responsible for the bending motion upon tactile sensation. Left: *D. capsensis* plant: Reproduced under terms of the CC-BY 3.0 CZ. Copyright 2006, Michal Rubeš. Right: Curled *D. capsensis* leaves: Reproduced under terms of the CC-BY 2.0. Copyright 2015, incidencematrix. Center: Schematics of inspired microanalytical system and its analyte capture mechanism with bicompartmental fibers triggered by pH. Bottom: State-of-the-art challenges due to mass transport limitations can be overcome by active transport of pH-responsive fibers: 1) Analyte landing off-site of detector. 2) Analyte transport toward the detector by pH-responsive fibers after stimulation. 3) Increased detectability of analyte.

detection patch. Designed as a spiderweb, the reconfigurable fibers draw their function from their bicompartmental architecture.
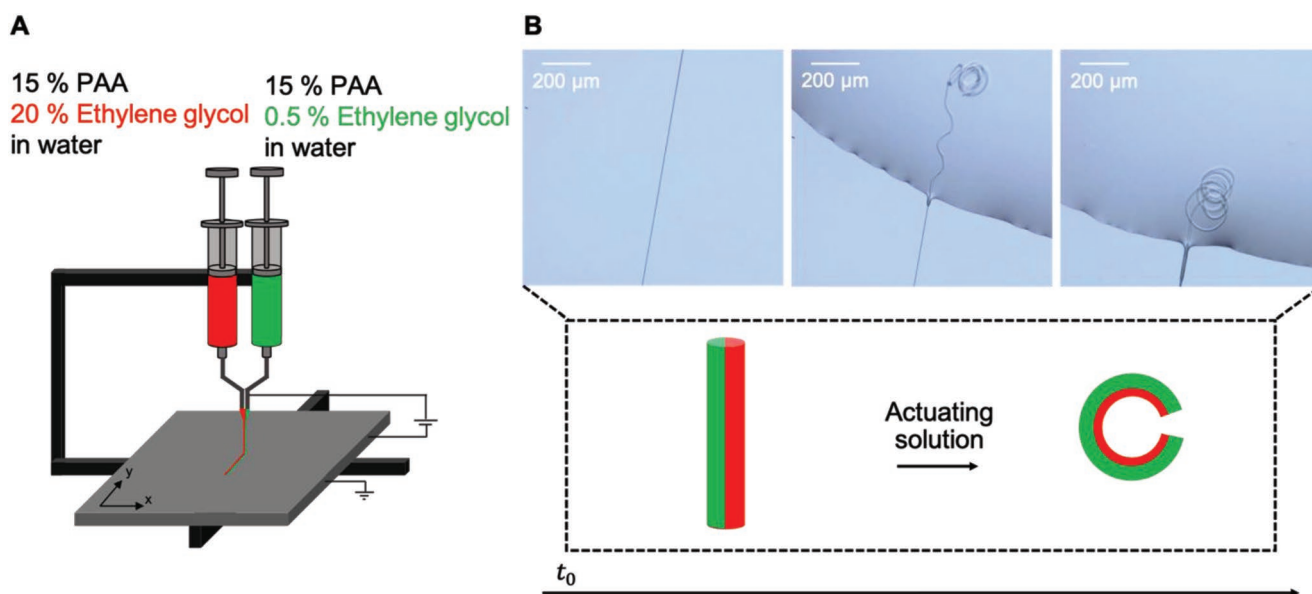
2. Results and Discussion

EHD co-jet writing is used to fabricate bicompartmental fibers made of poly(acrylic acid) (PAA), where the fiber architecture is characterized by two separate compartments with distinct swelling properties (Figure 1, center).[17,20] Under slightly acidic to neutral conditions, at pH values above 5.0, the acrylate groups are deprotonated, resulting in a differential swelling of the fiber compartments that gives rise to interfacial tension and ultimately results in shape reconfiguration. The active and direct analyte transport to the detector patch via reconfigurable fibers can overcome mass transport limitations currently faced within conventional microanalytical systems (Figure 1, bottom).[2a,4a,b] However, the shape reconfiguration of those fibers has to occur in a controlled manner to enable the directed transport of analyte particles. Therefore, the bicompartmental fibers were written into spiderweb-like network structures using 3D jet writing. In this work, we used a small sample volume with fluorescently-labeled microspheres to simulate an analyte: 1) The analyte in the sample solution lands onto the surrounding surface area of the detector. 2) The actuated

fibers transport the fluorescently-labeled spheres to the detector patch. 3) The increased analyte concentration enables the detection of the enhanced fluorescence intensity.

The experimental setup for EHD co-jet writing is shown in **Figure 2**. In brief, a high electric potential deforms the solution droplet at the needle tip into the so-called Taylor cone. An electrified fluid jet is ejected from the cone and accelerated toward the grounded collector plate. Unlike conventional electrospinning,[21] in which randomly nonwoven fiber mats are typically observed, we observed controlled deposition of defined and fully solidified fibers with a diameter of 5 μm. Two different polymer solutions were prepared by mixing 15.0% w/v PAA with ethylene glycol (EG, 0.5% v/v and 20.0% v/v for compartment A and B, respectively) in Milli-Q water. As reported elsewhere, EG has been used as crosslinker for PAA.[22] A control of electrojetted PAA fibers without EG dissolved after immersion in water, verifying EG's ability as a crosslinker. Due to the different EG concentration, each compartment has a different network density once the fibers are crosslinked. This asymmetric density is responsible for the different swelling properties upon the addition of an actuating solution (pH 7.0) (Figure 2B).

Confocal scanning laser microscopy (CLSM) was performed to visualize the bicompartmental PAA fibers (**Figure 3**A). Therefore, trace amounts of red (rhodamine B, ≈0.05 w/v%)

**ADVANCED
SCIENCE NEWS**

www.advancedsciencenews.com

**ADVANCED
FUNCTIONAL
MATERIALS**

www.afm-journal.de

Figure 2. Fabrication of pH-responsive polymer fibers via electrohydrodynamic co-jet writing. A) Schematic setup for bicompartmental fiber preparation via jet writing. B) Actuation mechanism due to anisotropic swelling. Scale bar 200 μm.

and green (fluorescein isothiocyanate [FITC], ≈0.05 w/v%) fluorescent dyes were loaded into the two jetting solutions. The polymer solution for compartment A consisted of the higher crosslinker concentration (20.0% v/v EG) compared to compartment B (0.5% v/v EG). Various pH buffers ranging from 3.0 to 9.0 were screened to determine which pH induces the greatest fiber actuation. Therefore, the swelling factor Q and curvature K were investigated. In Figure 3B, Q of one- and bicompartmental fibers were plotted as a function of pH and increased with pH as the carboxylic groups of PAA were ionized above its pKA value of 4.7.[23] Under strongly acidic conditions (pH <3.0), the carboxyl groups of the polymer network are protonated, screening the electrostatic repulsion between charged acid groups. As the pH increases, carboxylic acid groups within the network are deprotonated to negatively charged carboxylate ions, which results in electrostatic repulsion and causes the hydrogel to swell.[24] At pH 7.0, Q reaches a plateau, and a further increase in pH does not result in significant changes.[25] In terms of the higher EG concentration in compartment A, the crosslinker inhibited more significant hydrogel swelling compared to compartment B. At pH 7.0, compartment B swelled five times more than compartment A resulting in the greatest actuation and thus most significant curvature ($K = 19.0 \times 10^{-3}$ 1 per μm) (Figure 3C). As a control, the curvature of one-compartmental fibers was investigated. However, it was seen that one-compartmental fibers lack the ability to bend, meaning the curvature could not be measured. In Figure 3C, this is reflected by the bending radius R approaching infinity and the curvature equaling zero, demonstrating the necessity of bicompartmental fiber structures for bending motions.

Next, we analyzed the circularity c and the aspect ratio (AR) of shape reconfigured fibers for pH 7.0 and 9.0, as fibers did not fully reconfigure into circles at lower pH values. At pH 7.0, bicompartmental fibers reconfigured into a more circular shape ($c = 0.9 \pm 0.002$), than fibers in pH 9.0 ($c = 0.84 \pm 0.03$)

(Figure 3D). A circularity value of "1.0" indicates a perfect circle. A value approaching "0.0" indicates an increasingly elongated polygon. As for the aspect ratio, which considers the major and minor axes, fibers in pH 7.0 approach a circle ($AR = 1.07 \pm 0.03$), as $AR = 1$ applies to a circle (Figure 3E). In pH 9.0, on the other hand, the AR value is higher ($AR = 1.29 \pm 0.11$). We attribute these observations to the fact that the difference in swelling ratio between the PAA polymer containing 0.5% EG and the PAA polymer containing 20% EG is the largest at pH 7 and decreases again at higher pH (Figure 3B). Moving forward, the following experiments were performed at pH 7.0.

Moreover, the kinetics of the pH-induced curling was investigated by determining the strain ε of bicompartmental fibers, as a result of the bending motion (Figure 3F). Therefore, the bending radius R of the bicompartmental fibers was measured at various times while being exposed to the actuation solution. The fiber bending decreased with the solution immersing time. Once the fiber is saturated with water, the bending appears to stop. We speculate that this occurs due to the gradual water absorption saturation, which suggests that water is the driving force of the actuation. Thus, the bending strain exponentially increased with exposure time following the relationship $1 - \exp\left(-\dfrac{t}{\tau}\right)$, where t is time and τ is the time constant, which yielded $\tau = 0.16$ s. A curling fiber in solution can generate a force of 3.4 nN (Figure S1, Supporting Information).

The bicompartmental fibers were deposited in a spiderweb network geometry, in which all fibers overlapped each other at the center of the scaffold to create a 2.0×10^{-3} cm²-sized spot. The entire 1.5 cm diameter scaffold was centrally integrated within a 2.0×2.0 cm PDMS chamber. An induced pH change from 3.0 to 7.0 triggered the actuation of the fibers (**Figure 4**A). Due to the overlap of multiple fibers from various directions at one central point, the actuation direction was guided toward the center as that point was more stable during and after the
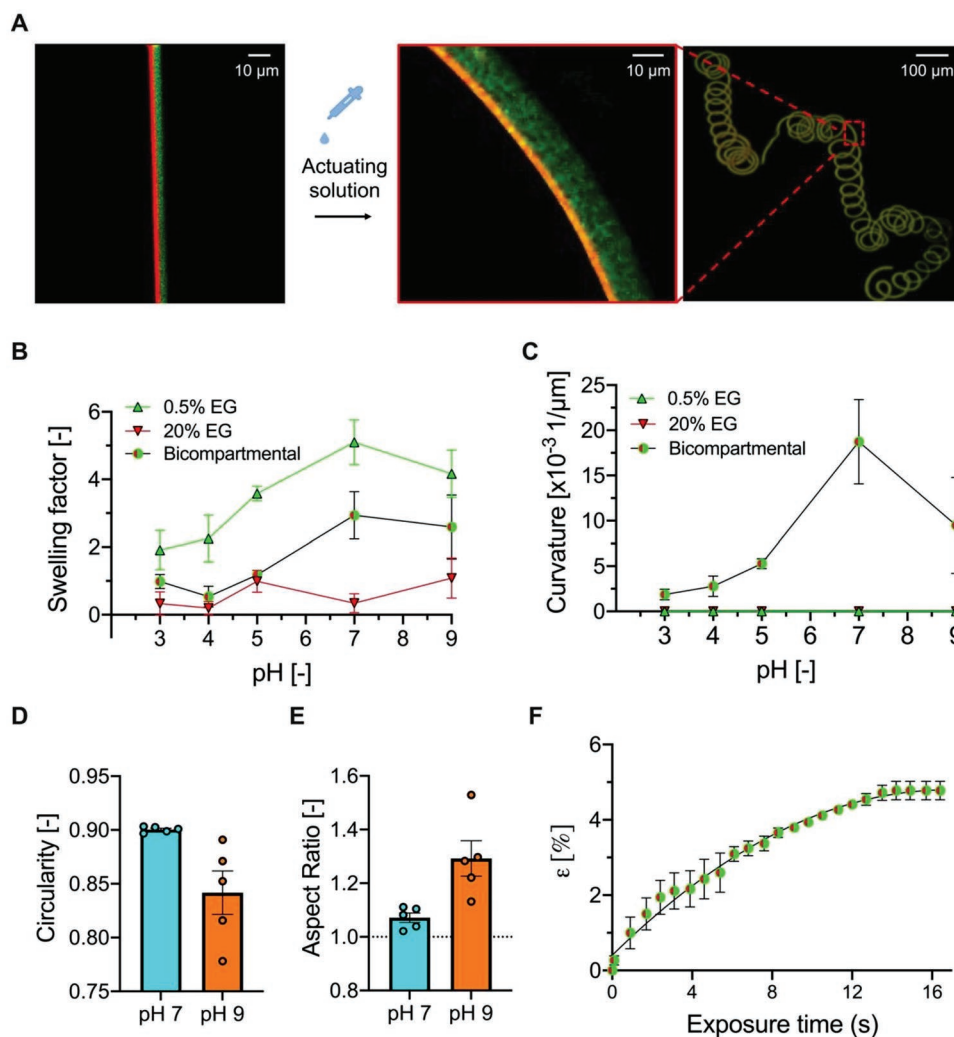
Figure 3. Actuation of pH-responsive fibers. A) Confocal images of bicompartmental poly(acrylic acid) (PAA) fiber. In red, compartment A with 20% ethylene glycol (EG); in green, compartment B with 0.5% EG. i) Before actuation. Scale bar 10 µm. ii,iii) After actuation. Compartment B swells five times more than compartment A. Scale bar 10 and 100 µm, respectively. pH-dependent B) swelling ($n = 5$ for all groups) and C) curvature ($n = 5$ for all groups). D) Circularity ($n = 5$ for all groups) and E) aspect ratio of reconfigured fibers ($n = 5$ for all groups). Aspect ratio value "1.0" indicating a circle. F) Bending strain of bicompartmental fibers ($n = 5$ for all groups). Data in (B)–(F) are represented as mean ± s.e.m.

actuation. The movement toward the scaffold center leads to the transport of randomly placed polystyrene microspheres (diameter $d = 10$ µm and $d = 200$ µm) that mimic an analyte to the small sensing area. The analyte deposition onto the spiderweb network increased the probability of analytes settling on fibers due to its large surface area coverage of 1.77 cm². Within $t \approx 240$ s, the fiber reconfiguration reduced the surface area coverage by 99% to a small sensing area of 0.02 cm². Transporting the analyte to a small sensing area increases the number of analytes detected per unit area and thus the sensitivity. A qualitative representation of relative surface area coverage of larger microspheres ($d = 200$ µm) over a relative time is shown in **Figure 5**C. At the beginning of the experiment ($t = 0$), all particles remained at their starting point and thus, had a maximum distance D to the center ($D = 1$). Once the actuating solution was added, the curling fibers moved their respective particles toward the center. On average, the fibers transported

the spherical particles 45% at $t = 0.25$. Thus, the relative surface area shrank by 70%. At $t = 1$, the surface area shrank to 7% of its initial size. Overall, the fibers did not transport the particles uniformly over the relative time resulting in an exponential decrease (Figure 5F). The transport of the smaller microspheres ($d = 10$ µm) followed the same trend, although to a much lesser extent. Moreover, fibers with 10 µm spheres moved more uniformly, similar to the control, which showed a linear and uniform decrease (Figure 5A,B,D,E).

Supporting the abovementioned findings of an inconsistent fiber movement with 200 µm spheres, their fiber velocity v had a wider distribution ($v = 46 \pm 12$ µm s^{-1}), compared to the one of the control ($v = 47 \pm 5$ µm s^{-1}) and fibers with 10 µm spheres ($v = 42 \pm 5$ µm s^{-1}) (Figure S2, Supporting Information). In all cases, the reconfigurable fibers enabled the fast surface area reduction. Conventional microanalytical systems, which lack the ability of a size-reducible sensing area, suffer from a
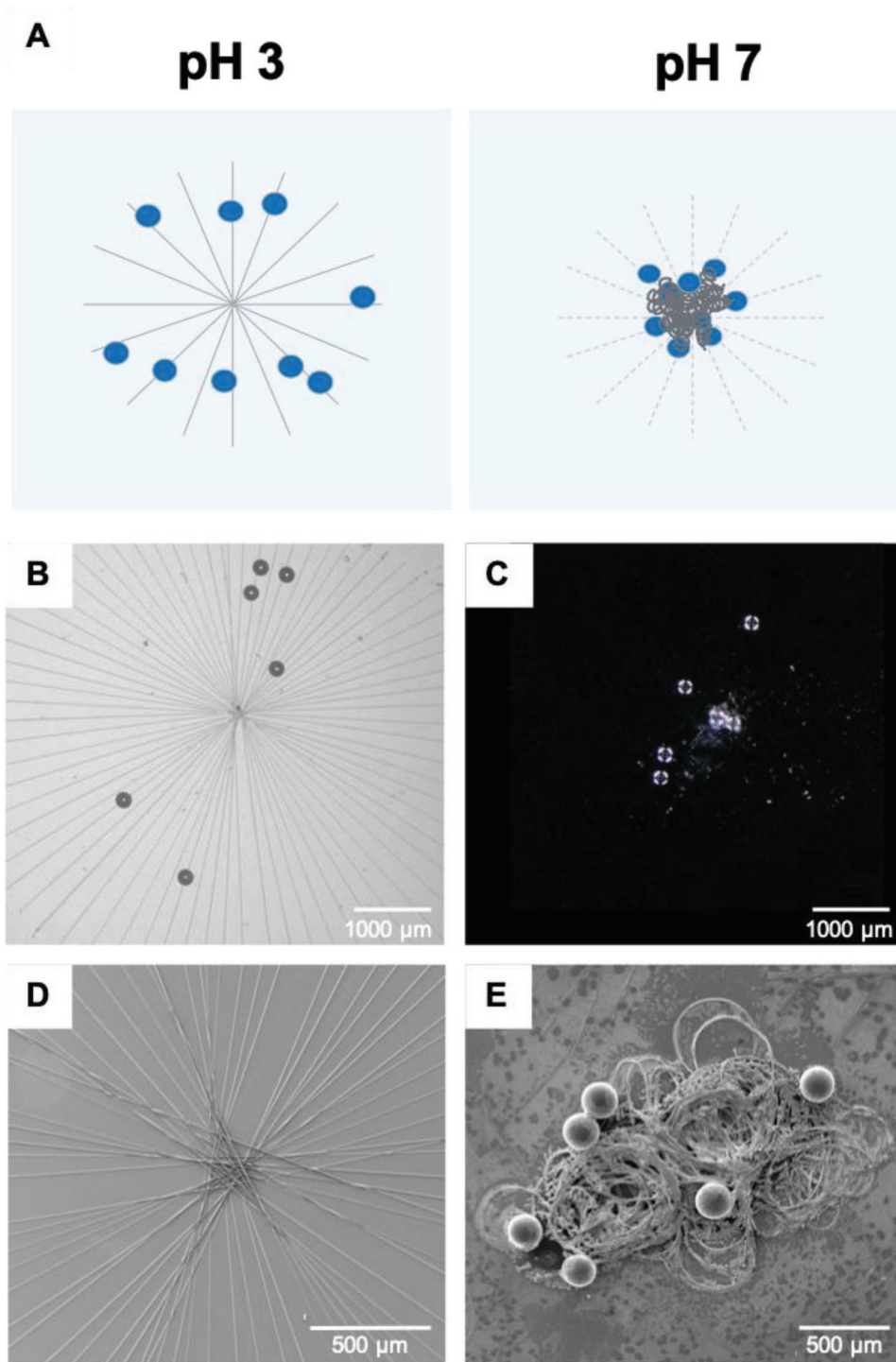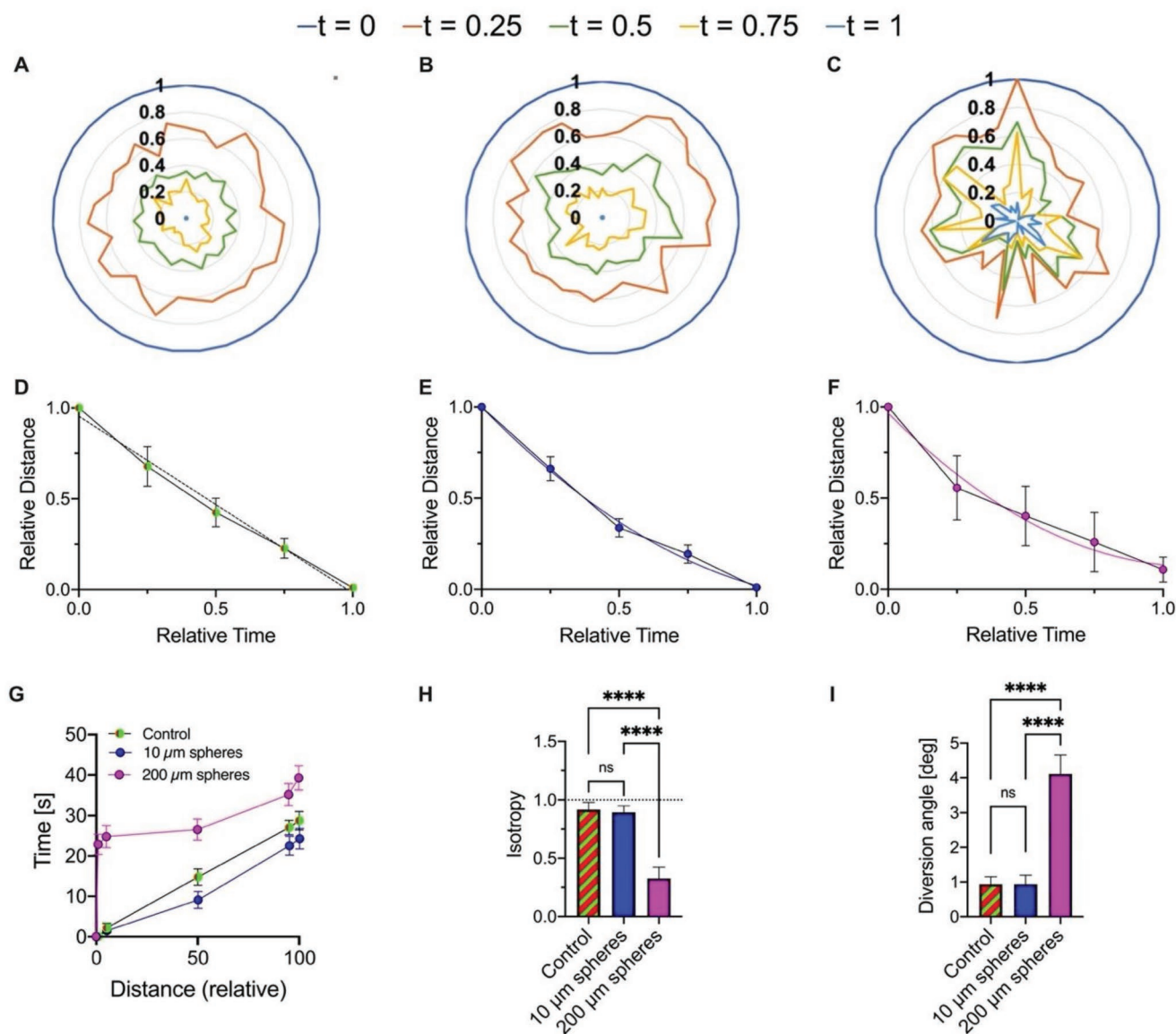
Figure 4. Directed transport for analyte collection. A) Schematic setup of the pH-responsive scaffolds and spheres within a chamber. Bright-field and SEM images of fiber structures and spheres before (B,D) and after (C,E) the actuation. Scale bar 1000 and 500 µm, respectively.

significantly low probability of analytes directly reaching the small sensing area.

The particle impact on the curling behavior of fibers was further assessed by investigating the actuation response. Compared to the control and 10 µm spheres, where the transport follows a linear curve, the transport of the 200 µm follows a sigmoidal curve (Figure 5G). The transport of 200 µm spheres delayed the fiber actuation response by nearly 23 s. Moreover, fibers transporting larger spheres follow a more undirected trajectory. This is shown in the lower isotropy $I = 0.33$ than the control ($I = 0.92$) and 10 µm spheres ($I = 0.89$) (Figure 5H). A maximum I "1.0" indicates highly ordered fiber movements. Compared to

2204080 (5 of 11)

ADVANCED
SCIENCE NEWS
www.advancedsciencenews.com

**ADVANCED**
FUNCTIONAL
MATERIALS
www.afm-journal.de

Figure 5. Particle transport due to fiber reconfiguration. Qualitative representation of relative surface area coverage of A) control, B) 10 µm, and C) 200 µm spheres over a relative time with the maximal and minimal distance D to the network center, $D = 1$ and $D = 0$, respectively. Quantitative representation of relative surface area coverage over a relative time of D) control, E) 10 µm, and F) 200 µm spheres. Trendline control ($y = -0.9724x + 0.9542$; $R^2 = 0.9902$), 10 µm spheres ($y = -0.9807x + 0.9318$; $R^2 = 0.9714$), 200 µm spheres ($y = 0.6076x^2 - 1.4141x + 0.938$; $R^2 = 0.9821$). G) Reconfiguration response of actuated fibers with 10 µm, 200 µm spheres, and control. H) Quantitative analysis of isotropy ($n = 30$ for all groups). Maximum isotropy value "1.0" indicating highly ordered fiber movements. I) Quantitative analysis of diversion angle ($n = 30$ for all groups). For (H) and (I), significant difference: ****$p < 0.0001$ (One-way ANOVA). Data in (D)–(I) are represented as mean ± s.e.m.

the control and smaller spheres, where the transport had a diversion angle DA of 0.94°, the transport with larger spheres had a significantly higher diversion angle ($DA = 2.63°$) (Figure 5I). The DA indicates the degree to which the fiber movement diverts from its initial trajectory. Thus, the fiber trajectory was significantly impacted by the 200 µm spheres, while no significant impact was seen with the smaller microspheres. Experiments with medium-sized polystyrene spheres ($d = 50$ µm) were also performed and the results are generally consistent with those reported with 200 µm spheres (Figure S3, Supporting Information). The 50 µm spheres have an impact on the fiber

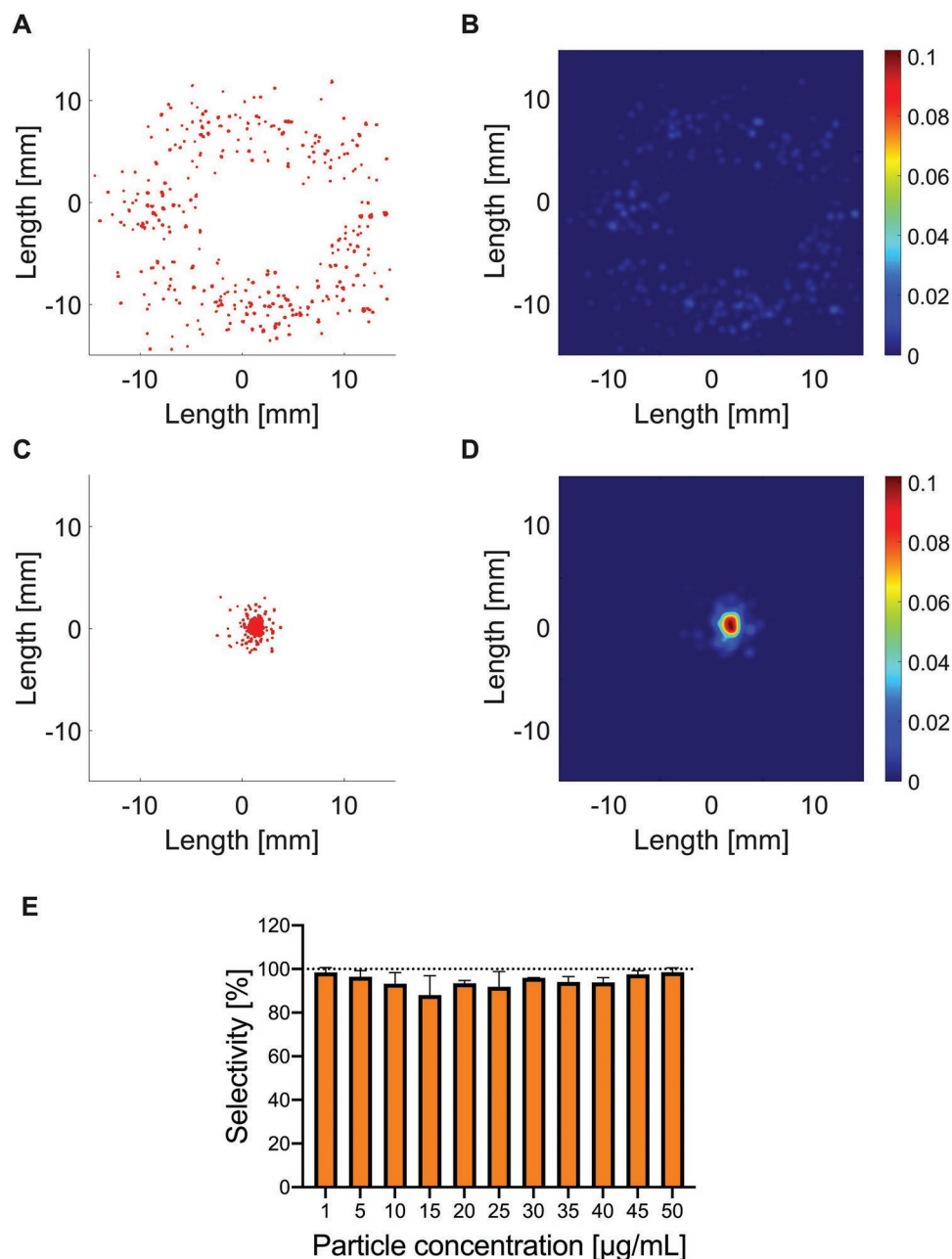reconfigurability ($DA = 3.46°$, I = 0.5) and follow the same trajectory as the 200 µm spheres, however, to a lesser extent.

Based on the ability of the scaffold to accumulate microspheres into the center, fluorescently-labeled spheres ($d = 10$ µm) were used to measure an increased fluorescent signal after the actuation. In the unreconfigurable state of a scaffold, no fluorescence was detectable from the randomly placed microspheres. Moreover, since the microspheres were widely scattered on the platform without any overlap (**Figure 6**A), no spatial density can be plotted in the 2D kernel density estimation plot (Figure 6B). After the actuation, an increase in the fluorescence intensity
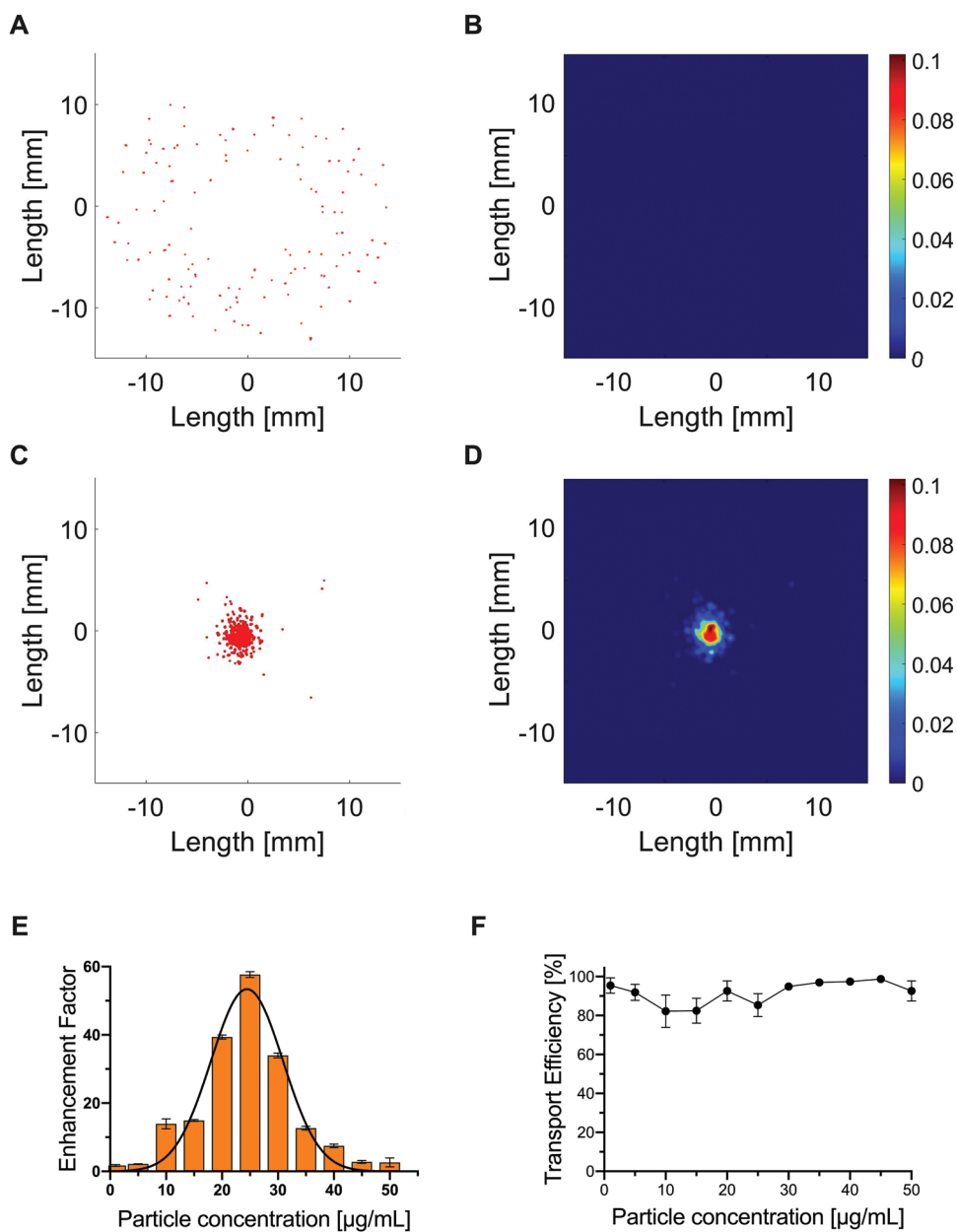
Figure 6. Increased fluorescence intensity due to enhanced analyte collection. Scatter plots and 2D Kernel density estimation plots of 10 μm spheres before (A,B) and after (C,D) the actuation. E) Fluorescent enhancement factor of spheres after actuation depending on the initial particle concentration ($c = 1, 5, 10, 15, 20, 25, 30, 35, 40, 45,$ and 50 μg mL^{-1}; $n = 3$ for all groups). F) Scaffold transport efficiency of spheres ($n = 3$ for all groups). Data in (E) and (F) are represented as mean ± s.e.m.

and spatial density was detectable, suggesting that the actuation actively increased the sensitivity and decreased the detection limit (Figure 6C,D). The fluorescence signal is directly proportional to the amount of sphere present in the sample. The more spheres are within the sample, the higher the signal that can be detected. The enhancement factor, which is the ratio of fluorescence signal detected after and before the direct transport, was, therefore, determined to analyze the efficiency of the analyte collection. In Figure 6E, the enhancement factor of various particle concentrations ($c = 1, 5, 10, 15, 20, 25, 30, 35, 40, 45,$ and 50 μg mL^{-1}) was plotted. The results fitted by Gaussian

distribution were also indicated (Mean = 25 μg mL^{-1}; amplitude = 53.4). The lowest particle concentration ($c = 1$ μg mL^{-1}) only had a 2-fold intensity enhancement. As expected, this was the lowest ratio amongst all concentrations. With a 5-fold intensity enhancement, the highest concentration ($c = 50$ μg mL^{-1}) achieved the second-lowest enhancement factor as the initial intensity in the unreconfigurable state was already high. The greatest enhancement factor with a 57-fold was measured for $c = 25$ μg mL^{-1}. Irrespective of the particle concentrations, randomly placed spheres were transported to the sensing area with a 91.9 ± 2.4% efficiency (Figure 6F).

**ADVANCED
SCIENCE NEWS**

www.advancedsciencenews.com

*ADVANCED
FUNCTIONAL
MATERIALS*

www.afm-journal.de

Figure 7. Analyte separation based on scaffold selectivity. Scatter and 2D Kernel density estimation plots of non-binding (A,B) and binding (C,D) spheres. E) Selectivity of binding and non-binding spheres ($n = 3$ for all groups). Non-binding concentration remained constant ($c = 10\,\mu g\,mL^{-1}$). Data in (E) are represented as mean ± s.e.m.

To assess the selectivity of the scaffolds, microspheres ($d = 10\,\mu m$) were simultaneously placed onto the scaffold. For non-binding spheres, the sphere surface was hydrophobically coated, while the binding spheres remained untreated. **Figure 7**A,B and 7C,D show scatter and 2D kernel density estimation plots of three sample overlays with non-binding and binding spheres, respectively. The non-binding spheres were not transported by the fibers. Instead, the non-binding spheres formed a torus shape after the actuation. In contrast, the binding spheres were all transported to the sensing area. The selectivity was investigated for various binding spheres concentration

($c = 1, 5, 10, 15, 20, 25, 30, 35, 40, 45,$ and $50\,\mu g\,mL^{-1}$), while the non-binding concentration remained constant at $c = 10\,\mu g\,mL^{-1}$. At all binding sphere concentrations, a significant separation from the non-binding spheres was achieved. The greatest selectivity with $98.6 \pm 2.0\%$, was achieved at a binding sphere concentration of $50\,\mu g\,mL^{-1}$. For all tested concentrations, the average separation efficiency of $95 \pm 3\%$ was achieved.

To evaluate the impact of complex environments on the network reconfiguration, experiments were repeated in 10% fetal bovine serum-based medium. Under these conditions, fiber reconfiguration was still observed (Figure S4, Supporting

Information). We also note that the ionic strength of blood, which is approximately 0.15 M,[26] lies within the range of ionic strengths (0.275 to 0.5 M), for which we observed robust fiber swelling (Figure S5, Supporting Information). For biosensing applications, future studies will need to investigate the sensitivity and specificity of the platform in presence of non-target proteins and other components within the sample solution. Such complex sample solutions might impact the fiber reconfigurability and consequently the detection function, as seen in biomolecular motor-based devices, which are impacted by undiluted blood samples.[27] Future studies should also evaluate the immobilization of more specific analytes that may be detected via immobilization of their respective binding partners into the polymer network after chemical vapor deposition (CVD) polymerization.[28] Further, since the analysis is based on optical measurements, limitations within the optical detection and resolution can impact analytical detection. With further work, reconfigurable polymer networks, such as the one discussed in this work, have the potential to actively transport and accumulate analyte in a detection patch.

3. Conclusions

We designed bicompartmental fiber networks capable of actively transporting analytes to the detector patch to address mass transport limitations within microanalytical systems. Our approach is based on the shape reconfigurable spiderweb network architectures fabricated by controlled fiber deposition via 3D jet writing. The specific geometry enables the directed movements of our reconfigurable fibers toward the network center, which bending motion is inspired by the carnivorous plant, *Drosera capensis*. As a proof of concept, we demonstrated the collection of particles from a large surface to a small sensing area for an improved detection resolution. This work establishes technological progress over conventional analytical methods concerning flexibility, specificity, and the application of cheaper materials. Due to the ability of directed transport, our platform has the potential to drive small-scale biosensors to the forefront of microanalytical methods.

4. Experimental Section

Materials: All chemicals and lab supplies were obtained from VWR unless otherwise mentioned. PAA ($M_w = 450\,000$ g mol^{-1}) was purchased from Sigma Aldrich. Ethylene glycol (Emplura, Merck Millipore, USA), Potassium dihydrogen phosphate (≥99.0% ACS, Fluka, Honeywell Chemicals, USA), Sylgard 184 (PDMS, Dow Corning Corporation, USA), MF-FluoBlue 9.8 and PS-R-214.0 (microparticles GmbH, Germany), Fluoresbrite YG Carboxylate Polystyrene (PS) Microspheres (10 μm diameter, Polysciences, Inc., USA), and silicon wafers with a native oxide layer (Siegert Wafer GmbH, Germany) were also used in the experiments.

EHD Co-Jet Writing: Scaffolds made of bicompartmental fibers were fabricated using the EHD co-jetting procedure. Therefore, two jetting solutions of 15% (weight per volume, w/v) polyacrylic acid (PAA) in Milli-Q water were prepared with different ethylene glycol concentrations (0.5% and 20% volume per volume, v/v). A syringe pump (LA-110, Landgraf HLL GmbH, Germany) with a flow rate of 20 μL per hour was set to flow the two polymeric solutions in a laminar regime through parallel metallic needles (25G, ID = 0.84 mm, Nordson EFD,

USA). An external power source (FuG Elektronik, Germany) charged the needles to −1.9 kV. The grounded collector plate was mounted on a computer-assisted x–y stage (Newport Corporation, USA). The x–y stage was controlled by software (Direct Machining Control, Lithuania) that precisely placed the stable polymer jet into pre-programmed structures. The distance between the needles and the collector plate was kept constant at 0.5 cm. Fibers were jetted on dimethyloctadecyl[3-(trimethoxysilyl)propyl] ammonium chloride (DMOAP)-coated silicon wafers, which were placed on top of the collector plate. For samples examined with the confocal microscope, glass slides were used.

Scanning Electron Microscopy: For SEM imaging the samples were sputter-coated with an approximately 5 nm gold–palladium [80:20] layer to improve the conductivity using a MED 020 device (Bal-Tec AG, Balzers, Liechtenstein). SEM images were obtained using a VEGA 3 (TESCAN, Germany) at 8.0 kV.

Swelling Properties: The swelling factor Q of the fibers (one-compartment; bicompartmental) was determined in the following pH values 3.0, 4.0, 5.0, 7.0, 9.0. All solutions had a molarity of 0.1 M and an ionic strength of 0.265 M. Therefore, the fiber diameters ($n = 5$) were measured in a dry d_d and swollen d_s state after being immersed in the respective solution overnight. The swelling factor Q was calculated with the following equation:

$$Q = \frac{d_s - d_d}{d_d} \tag{1}$$

The curvature K of bicompartmental fibers was determined in the following pHs 3.0, 4.0, 5.0, 7.0, 9.0. The bending radius R was measured with ImageJ for the following equation:

$$K = \frac{1}{R} \tag{2}$$

The circularity c of the bicompartmental fibers was determined in the following pH values 7.0 and 9.0 with ImageJ that uses the following equation:

$$c = \frac{4\pi A}{p^2} \tag{3}$$

For the aspect ratio AR of the bicompartmental fibers the major and minor axes were determined in the following pH values 7.0 and 9.0 with ImageJ and calculated using the following equation:

$$AR = \frac{d_{major}}{d_{minor}} \tag{4}$$

The bending strain of bicompartmental fibers were determined over time. Therefore, the fiber radius r_f and bending radius R were measured with ImageJ for the following equation:

$$\varepsilon = \frac{r_f}{R} \tag{5}$$

Analyte Transport Experiment: A chamber-like construction that consisted of a glass coverslip and PDMS strips was placed onto the scaffold and filled with a non-actuating solution (pH 3.0). With a pipette, 10 μL of the microparticle suspension ($c = 1, 5, 10, 15, 20, 25, 30, 35, 40, 45,$ and 50 μg mL^{-1}) was added onto the scaffold. Once the entire chamber was filled, the acidic solution was slowly replaced with the actuating solution (pH 7.0). Therefore, two syringe pumps, one from the top, the other one from the bottom were used to ensure laminar flow. A third syringe pump withdrew the solution from the site. All syringes were operated with syringe pumps at flow rates of 40 and 80 μL per hour, respectively. For separation experiments, non-binding spheres were prepared by immersing FITC carboxylated polystyrene particles in 3–5% DMOAP (60% in methanol) for 10 min and washed with Mili-Q water afterward.

Light Microscopy: The curling experiments were analyzed under a BX53 Olympus microscope for both bright-field and fluorescence imaging. All images and videos were processed and further analyzed with ImageJ.

Diversion Angle and Isotropy: All videos were processed with MATLAB for further analysis. TrackMate, a particle tracking plug-in for ImageJ, was used to measure the particle position for each video frame and track its path. The diversion angle was determined by measuring the angle of the unactuated fiber against the tracked particle path after actuation. With another ImageJ plug-in, FibrilTool, the anisotropy of fibers and fibers with spheres was analyzed by selecting the tracked particle path as region of interest (ROI; yellow). An isotropy of "0.0" indicated purely anisotropic arrays, while a score of "1.0" showed a perfectly ordered fiber movement.

Statistical Analyses: Statistical significance was analyzed using one-way analysis of variance with Tukey's multiple-comparison test. *p*-Values represent different levels of significance; $p < 0.05$ *; $p < 0.01$ **; $p < 0.001$ ***; $p < 0.0001$ ****. All data analysis was carried out with Graphpad Prism v9.0.

Conflict of Interest

The authors declare no conflict of interest.

Data Availability Statement

The data that support the findings of this study are available from the corresponding author upon reasonable request.

[1] a) D. R. Reyes, D. Iossifidis, P.-A. Auroux, A. Manz, *Anal. Chem.* **2002**, *74*, 2623; b) Y. Song, B. Lin, T. Tian, X. Xu, W. Wang, Q. Ruan, J. Guo, Z. Zhu, C. Yang, *Anal. Chem.* **2018**, *91*, 388; c) F. Wieland, R. Bruch, M. Bergmann, S. Partel, G. A. Urban, C. Dincer, *Polymers* **2020**, *12*, 104; d) P. R. Coulet, L. J. Blum, *Biosensor Principles and Applications*, CRC Press, Boca Raton, FL **2019**.

[2] a) A. Sitt, H. Hess, *Nano Lett.* **2015**, *15*, 3341; b) P. Katira, H. Hess, *Nano Lett.* **2010**, *10*, 567.

[3] a) M. Lin, J. Wang, G. Zhou, J. Wang, N. Wu, J. Lu, J. Gao, X. Chen, J. Shi, X. Zuo, *Angew. Chem.* **2015**, *127*, 2179; b) X. Qu, F. Yang, H. Chen, J. Li, H. Zhang, G. Zhang, L. Li, L. Wang, S. Song, Y. Tian, *ACS Appl. Mater. Interfaces* **2017**, *9*, 16026.

[4] a) R. J. White, H. S. White, in *A Random Walk Through Electron-Transfer Kinetics*, **2005**, p. 214-A; b) P. E. Sheehan, L. J. Whitman, *Nano Lett.*

[5] T. Nitta, H. Hess, *Cell Mol. Bioeng.* **2013**, *6*, 109.

[6] a) S. Ramachandran, K. H. Ernst, G. D. Bachand, V. Vogel, H. Hess, *Small* **2006**, *2*, 330; b) D. Inoue, T. Nitta, A. M. R. Kabir, K. Sada, J. P. Gong, A. Konagaya, A. Kakugo, *Nat. Commun.* **2016**, *7*, 12557; c) A. J. Wollman, C. Sanchez-Cano, H. M. Carstairs, R. A. Cross, A. J. Turberfield, *Nat. Nanotechnol.* **2014**, *9*, 44.

[7] a) T. J. Grove, K. A. Puckett, N. M. Brunet, G. Mihajlovic, L. A. McFadden, P. Xiong, S. von Molnár, T. S. Moerland, P. B. Chase, *IEEE Trans. Adv. Packag.* **2005**, *28*, 556; b) R. Seetharam, Y. Wada, S. Ramachandran, H. Hess, P. Satir, *Lab Chip* **2006**, *6*, 1239; c) M. A. Rahman, C. Reuther, F. W. Lindberg, M. Mengoni, A. Salhotra, G. Heldt, H. Linke, S. Diez, A. Månsson, *Nano Lett.* **2019**, *19*, 7155; d) L. Hines, K. Petersen, G. Z. Lum, M. Sitti, *Adv. Mater.* **2017**, *29*, 1603483; e) M. Lard, L. Ten Siethoff, S. Kumar, M. Persson, G. Te Kronnie, H. Linke, A. Månsson, *Biosens. Bioelectron.* **2013**, *48*, 145.

[8] a) S. Zhang, S. J. Kieffer, C. Zhang, A. G. Alleyne, P. V. Braun, *Adv. Mater.* **2018**, *30*, 1803140; b) N. Yonet-Tanyeri, R. C. Evans, H. Tu, P. V. Braun, *Adv. Mater.* **2011**, *23*, 1739; c) H.-J. Koo, K. V. Waynant, C. Zhang, P. V. Braun, *ACS Appl. Mater. Interfaces* **2014**, *6*, 14320; d) T. H. Tsai, M. A. Ali, Z. Jiang, P. V. Braun, *Angew. Chem., Int. Ed.* **2017**, *56*, 5001; e) S. Zhang, C. Zhang, H. Chen, S. J. Kieffer, F. Neubrech, H. Giessen, A. G. Alleyne, P. V. Braun, *Angew. Chem.* **2019**, *131*, 18333.

[9] S. M. Desai, R. Singh, in *Long Term Properties of Polyolefins*, Springer, Berlin **2004**, p. 231.

[10] J. M. Goddard, J. Hotchkiss, *Prog. Polym. Sci.* **2007**, *32*, 698.

[11] a) N. Inagaki, *Plasma Surface Modification and Plasma Polymerization*, CRC Press, Boca Raton, FL **2014**; b) S. Morgenthaler, C. Zink, N. D. Spencer, *Soft Matter* **2008**, *4*, 419.

[12] a) D. P. Holmes, A. J. Crosby, *Adv. Mater.* **2007**, *19*, 3589; b) K. Efimenko, M. Rackaitis, E. Manias, A. Vaziri, L. Mahadevan, J. Genzer, *Nat. Mater.* **2005**, *4*, 293; c) L. Ionov, *Adv. Funct. Mater.* **2013**, *23*, 4555.

[13] C. A. La Porta, M. C. Lionetti, S. Bonfanti, S. Milan, C. Ferrario, D. Rayneau-Kirkhope, M. Beretta, M. Hanifpour, U. Fascio, M. Ascagni, *Proc. Natl. Acad. Sci. USA* **2019**, *116*, 18777.

[14] a) S. Zakharchenko, N. Puretskiy, G. Stoychev, M. Stamm, L. Ionov, *Soft Matter* **2010**, *6*, 2633; b) G. Stoychev, S. Zakharchenko, S. Turcaud, J. W. Dunlop, L. Ionov, *ACS Nano* **2012**, *6*, 3925; c) H. Lee, C. Xia, N. X. Fang, *Soft Matter* **2010**, *6*, 4342; d) Y. Ma, Y. Zhang, B. Wu, W. Sun, Z. Li, J. Sun, *Angew. Chem.* **2011**, *123*, 6378; e) G. Stoychev, S. Turcaud, J. W. Dunlop, L. Ionov, *Adv. Funct. Mater.* **2013**, *23*, 2295; f) K. Suzumori, S. Endo, T. Kanda, N. Kato, H. Suzuki, Proc. 2007 IEEE Int. Conf. on Robotics and Automation, IEEE, Piscataway, NJ **2007**; g) P. Polygerinos, Z. Wang, J. T. Overvelde, K. C. Galloway, R. J. Wood, K. Bertoldi, C. J. Walsh, *IEEE Trans. Rob.* **2015**, *31*, 778.

[15] K. Balani, V. Verma, A. Agarwal, R. Narayan, *Biosurfaces: A materials Science and Engineering Perspective*, John Wiley & Sons, New York **2015**.

[16] a) Y. Zhang, L. Ionov, *Langmuir* **2015**, *31*, 4552; b) A. Kirillova, R. Maxson, G. Stoychev, C. T. Gomillion, L. Ionov, *Adv. Mater.* **2017**, *29*, 1703443; c) G. Stoychev, C. Reuther, S. Diez, L. Ionov, *Angew. Chem.* **2016**, *128*, 16340.

[17] S. Moon, M. S. Jones, E. Seo, J. Lee, L. Lahann, J. H. Jordahl, K. J. Lee, J. Lahann, *Sci. Adv.* **2021**, *7*, eabf5289.

[18] J.-W. Yoo, S. Mitragotri, *Proc. Natl. Acad. Sci. USA* **2010**, *107*, 11205.

[19] a) K. J. Lee, J. Yoon, S. Rahmani, S. Hwang, S. Bhaskar, S. Mitragotri, J. Lahann, *Proc. Natl. Acad. Sci. USA* **2012**, *109*, 16057; b) J. Lee, T. H. Park, K. J. Lee, J. Lahann, *Macromol. Rapid Commun.* **2016**, *37*, 73.

[20] a) K.-H. Roh, D. C. Martin, J. Lahann, *Nat. Mater.* **2005**, *4*, 759; b) J. Lee, S. Moon, Y. B. Han, S. J. Yang, J. Lahann, K. J. Lee, *Macromol. Rapid Commun.* **2022**, *43*, 2100560.

[21] a) C. Chang, K. Limkrailassiri, L. Lin, *Appl. Phys. Lett.* **2008**, *93*, 123111; b) T.-S. Kim, Y. Lee, W. Xu, Y. H. Kim, M. Kim, S.-Y. Min, T. H. Kim, H. W. Jang, T.-W. Lee, *Nano Energy* **2019**, *58*, 437; c) C. Chang, V. H. Tran, J. Wang, Y.-K. Fuh, L. Lin, *Nano Lett.* **2010**, *10*, 726.

[22] a) J. Nie, Z.-l. Wang, J.-f. Li, Y. Gong, J.-x. Sun, S.-g. Yang, *Chin. J. Polym. Sci.* **2017**, *35*, 1001; b) L. Meng, W. Klinkajon, P.-r. K-hasuwan, S. Harkin, P. Supaphol, G. E. Wnek, *Polym. Int.* **2015**, *64*, 42.

[23] a) M. Fukushima, K. Tatsumi, S. Wada, *Anal. Sci.* **1999**, *15*, 1153; b) L. F. Gudeman, N. A. Peppas, *J. Membr. Sci.* **1995**, *107*, 239.

[24] a) T. Anirudhan, S. Rejeena, *Chem. Eng. J.* **2012**, *187*, 150; b) R. da Silva, M. G. de Oliveira, *Polymer* **2007**, *48*, 4114.

[25] a) W. A. Laftah, S. Hashim, *J. Compos. Mater.* **2014**, *48*, 555; b) S. J. Kim, K. J. Lee, S. M. Lee, I. Y. Kim, S. I. Kim, *High Perform. Polym.* **2004**, *16*, 625.

[26] A. Covington, R. Robinson, *Anal. Chim. Acta* **1975**, *78*, 219.

[27] S. Korten, N. Albet-Torres, F. Paderi, L. ten Siethoff, S. Diez, T. Korten, G. te Kronnie, A. Månsson, *Lab Chip* **2013**, *13*, 866.

[28] a) J. Lahann, W. Plüster, D. Klee, H.-G. Gattner, H. Höcker, *J. Mater. Sci.: Mater. Med.* **2001**, *12*, 807; b) H. Nandivada, H. Y. Chen, J. Lahann, *Macromol. Rapid Commun.* **2005**, *26*, 1794.